

(110) Facet of MgTe Zinc Blende Semiconductor: A Holy Grail for Modern Spintronics

Manish Kumar Mohanta* and Puru Jena*

Department of Physics, Virginia Commonwealth University, Richmond, VA 23284, USA

*E-mail: manishkmr484@gmail.com, mohantamk@vcu.edu, pjena@vcu.edu

In this work, we propose mono/few layers of MgTe (110) facets of zinc-blende structure for a unique next-generation ferromagnet-free nonballistic spin-field effect transistor. The atomic arrangement in this facet exhibits a unique combination of three basic symmetries found in nature: rotation, reflection, and translation. The electronic properties based on the density functional theory (DFT) reveal momentum-independent unidirectional spin polarization known as persistent spin texture (PST) that leads to an infinite spin lifetime in this particular facet. PST in these 2D structures originating from crystal symmetry makes them an ideal alternative to quantum well structures. Although the proposed Datta-Das s-FET is applicable to nonballistic s-FET, there has been little technological progress in this rapidly growing field of research and only a trivial amount of 2D semiconductors have been identified that exhibit PST intrinsically. In this regard, this particular facet studied in this work will be a great asset. A detailed theoretical insight into the origin of PST and its application in a ferromagnet-free s-FET has been proposed combining both the spin-Hall effect and inverse spin-Hall effects, harmonizing spintronics with conventional electronics.

1. Introduction

The spin of an electron is a fundamental property that originates from the electron's spinning around its axis. Its precise control for data storage and process has been of great interest and a hot topic of research following the proposal of a spin field effect transistor (s-FET) by Datta and Das.¹⁻³ The s-FET device consists of a lateral semiconducting channel exhibiting strong spin-orbit-coupling (SOC) and two ferromagnets used for spin generation and detection. The spin transport is controlled by the gate voltage in the semiconducting region. Depending on the spin-transport, ballistic (impurity-free) and non-ballistic s-FETs have been proposed but the latter have been less explored. In ballistic s-FET, the spin direction is maintained in the channel without any scatterings. The nonmagnetic Rashba semiconductors exhibit momentum-dependent Rashba spin splitting and are thus prone to impurity scattering in a non-ballistic region. However, spin-orbit interaction can be engineered to produce momentum-independent unidirectional spin configuration which is also known as persistent spin texture. This has been theoretically shown in a two-dimensional quantum well system having equal Rashba and Dresselhaus strength.^{4,5} Under this condition, enforced by SU(2) symmetry⁶ spins exhibit an extraordinarily long lifetime even in the presence of disorder or imperfection. Experimentally, the PST has been observed in quantum well structures⁷⁻¹⁰ having a channel length of order micrometer and, hence, there is a surge in interest to explore new 2D materials for designing atomic scale spintronic devices. The spin-helix state in a two-dimensional electron gas system is found to be robust against D'yakonov-Perel's spin relaxation in earlier work which makes Datta-Das type s-FET operable in the nonballistic transport regime.¹¹ For a conventional s-FET, interfacial scattering, band mismatch, ferromagnetic materials with 100% spin-polarized current, spin injection efficiency, and long spin lifetime¹² are some of the major challenges that hinder realizing actual s-FET devices. The control of spin precession using gate voltage requires channel semiconductors having large SOC in ballistic s-FET. However, recent work by Eberle et al.¹³ has demonstrated the use of relatively low SOC quantum well structures for a nonballistic s-FET. Although quantum well structures have been used for nonballistic s-FET under the stringent condition of equal Rashba and Dresselhaus constants, it is necessary to search for new materials that exhibit intrinsic PST.

Recently Tao and Symal have proposed a particular symmetry of a bulk crystal structure that belongs to the non-symmorphic space group exhibiting PST intrinsically.¹⁴ This work has generated a surge in interest to explore 2D materials that can exhibit the same properties enforced by symmetry. In this regard there are only a handful of 2D semiconductors that have been identified to exhibit PST to date; MX monolayers (M: Sn, Ge, X: S/Se/Te)¹⁵⁻¹⁷, Bi(110) monolayer¹⁸. In this work, we propose a unique composition of light (Mg) with a heavy (Te) element; MgTe (110) facet which is a direct band gap semiconductor having band edges located at the Γ -point. The PST is shown to exhibit at the Brillouin zone center and being a century-old semiconductor the experimental synthesis^{19,20} is widely known for this particular facet which makes these semiconductors very interesting and appealing to explore in nonballistic s-FET.

2. Results and Discussion

2.1 Symmetry analysis of MgTe (110) facets and ferroelectricity

The cubic zinc-blende (ZB) structure of MgTe has many facets having different atomic arrangements. A brief crystallographic description of different facets of the MgTe ZB structure is provided in Table 1 and their geometrical view is presented in Figure S1 in Supporting Information (SI). In this work we are particularly interested in the (110) facet of MgTe that belongs to the non-symmorphic space group which stands out from the other facets as the atomic arrangements in it show all three basic types of transformation rotation (R), reflection (M) and translation (t). The crystallographic coordinate transformation involves rotation (R) and translation (t) and can be written in the form of $\{R|t\}$. The mirror reflection symmetry can be obtained by roto-inversion symmetry operation, i.e., rotation followed by inversion.²¹ The translation vector (t) is zero for the symmorphic space group. Recently discovered black phosphorene is a typical example of a non-symmorphic space group. The physics of large systems can often be understood from the properties of the basic building block which, for the (110) facet, is depicted by a two-atomic thick layer (see Figure S1(d)). Hence, instead of studying multi-layer systems, the focus here is to analyze and explore the symmetry-dependent properties associated with the two-atomic (2L) thick MgTe layer. The top and side view of 2L-MgTe is plotted in Figure 1. Considering the two-dimensional MgTe system, the crystallographic symmetry operations under which the 2D structure remains invariant are represented in eq. (1); (i) identity operation E , (ii) one 2-fold rotation (180-degree) about the x -axis (C_{2x}) followed by a translation of $\{\frac{a}{2}, \frac{b}{2}\}$, (iii) one mirror symmetry in M_{zx} , (iv) one glide reflection \bar{M}_{xy} (mirror symmetry operation M_{xy} followed by translation $\{\frac{a}{2}, \frac{b}{2}\}$) and are pictorially illustrated in Figure 2.

$$\{< Ee| \{0,0,0\} >, < C_{2x}| \{\frac{a}{2}, \frac{b}{2}, 0\} >, < M_{zx}| \{0,0,0\} >, < \bar{M}_{xy}| \{\frac{a}{2}, \frac{b}{2}, 0\} >\} \dots (1)$$

Here, a and b are the lattice constants.

Table 1 Crystallographic information on various facets of zinc-blend bulk MgTe structure					
Facets	Space group no.	System	Schoenflies notation	International	Symmorphic
Bulk zinc-blende	216	Cubic	T_d^2	$F\bar{4}3m$	Yes
(100)/(001)	115	Tetragonal	D_{2d}^5	$P\bar{4}m2$	Yes
(111)	156	Trigonal	C_{3v}^1	$P3m1$	Yes
(110)	31	Orthorhombic	C_{2v}^7	$Pmn2_1$	No

Since the symmetry-dependent properties will be discussed in this work, any structural perturbations are excluded. The two-unit cells having opposite ferroelectric polarization MgTe

($+\vec{P}_x$) and MgTe ($-\vec{P}_x$) are designed to account for the effect of ferroelectric polarization on the electronic properties which will be discussed later. A built-in ferroelectric polarization originating from the nonsymmorphic element and broken inversion symmetry exists in the crystal structure. The ferroelectric polarization is calculated to be of magnitude 0.98×10^{-10} C/m which is comparable and much less than that of other previous reports Bi(110) (0.47×10^{-10})¹⁸, CdTe and ZnTe monolayers ($\sim 2.3 \times 10^{-10}$)²¹.

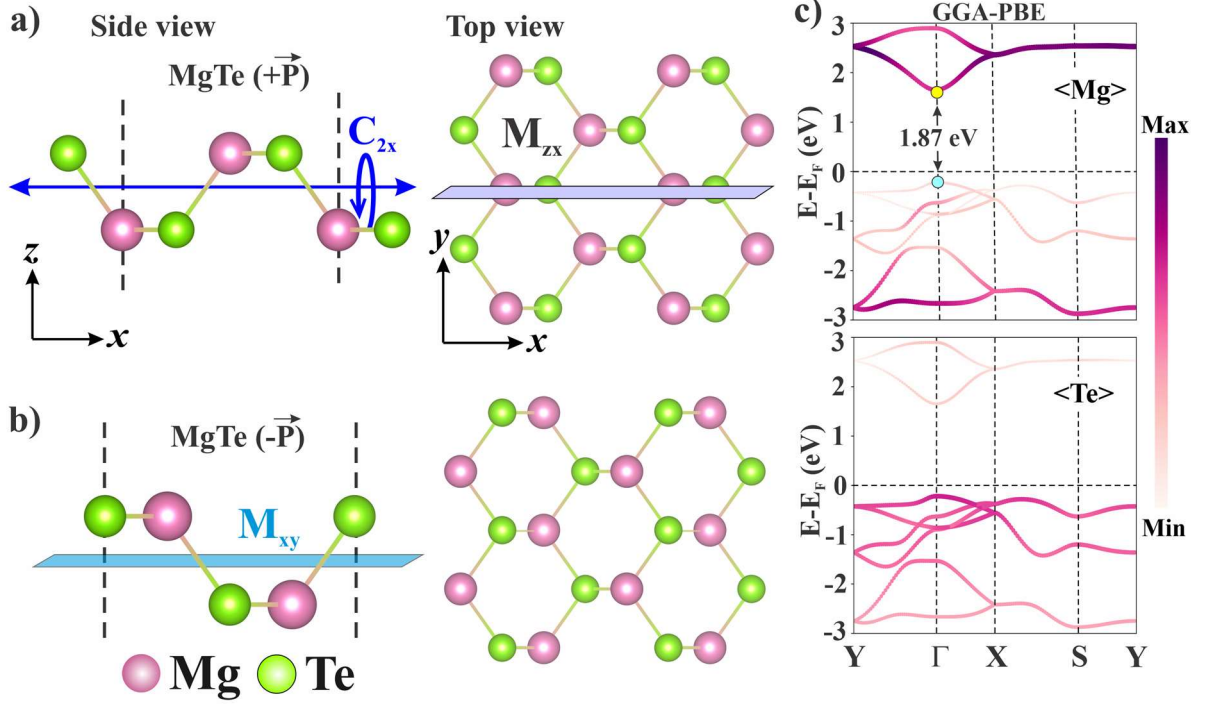


Figure 1 Top and side view of designed unit-cells having ferroelectric polarization opposite to each other (a) MgTe ($+\vec{P}_x$) and (b) MgTe ($-\vec{P}_x$) and (c) atom projected electronic band structure without including relativistic effect along high symmetry points of rectangular Brillouin zone $Y(0,0.5) \rightarrow \Gamma(0,0) \rightarrow X(0.5,0) \rightarrow S(0.5,0.5) \rightarrow Y(0,0.5)$; band edges are indicated by coloured circles.

2.2 Electronic band structure and persistent spin texture (PST)

The electronic properties are evaluated using the density functional theory (DFT). The electronic band dispersion of 2L MgTe is plotted in Figure 1(c) which depicts MgTe to be a direct band gap semiconductor of 1.87 eV having band edges located at the Brillouin zone centre Γ -point. The atom-projected band structure shows the contribution of each atom at the band edges. The atomic contribution of valence band maximum (VBM) is Mg (5.6%), Te (94.4%) whereas that of conduction band minimum (CBM) is Mg (36.22 %), Te (63.77 %). Since these structures are composed of heavy Te-atom, the effect of spin-orbit coupling (SOC) is reflected in the band structure plotted in Figure 2. A Rashba-type spin splitting is observed in Figure 2(a) which lifts the spin degeneracy (energy states corresponding to spin-up and spin-down) along $\Gamma \rightarrow Y$ direction whereas $\Gamma \rightarrow X$ direction remains degenerate. A spin degenerate

line node (SDLN) appears along the line $k_x = 0$ parallel to the ferroelectric polarization. The Rashba constant at both band edges is calculated from the band structure²² using eq. (2); $\alpha_R^{CBM} = 0.47 \text{ eV\AA}$, $\alpha_R^{VBM} = 1.44 \text{ eV\AA}$.

$$\alpha = \frac{2E_R}{k_R} \dots\dots\dots (2)$$

where E_R is the energy difference between the CBM/VBM and band crossing the Γ -point and k_R is the momentum offset.^{23,24} The Rashba constant at CBM is calculated for MgTe (110) is three times smaller compared to CdTe/ ZnTe (110) semiconductors. The difference in Rashba splitting at both CBM and VBM can be described from the band edge compositions of Te-atomic orbitals. Since CBM is composed of significant Mg-atomic orbitals the effect of Rashba splitting is lower compared to VBM. Furthermore, the spin-projected band structure confirms that the band edges are contributed by an out-of-plane spin component (S_z). This is different from the conventional Rashba effect where the in-plane components of spin (S_x, S_y) dominate at the Γ -point.²³⁻²⁷ This type of spin splitting is referred to as out-of-plane Rashba spin splitting where the spins are momentum-independent and unidirectional along the $\pm z$ direction which can be seen from the spin texture plot in Figure 2(c-d). This peculiar spin polarization in momentum space yields a specific spin-wave mode called persistent spin helix (PSH) which protects the spin from decoherence in a diffusive transport regime which, in turn, leads to an infinite spin lifetime.^{4,14,18,28} The shifting of parabolic energy dispersion ($\vec{Q} = \frac{2m\alpha}{\hbar^2} \hat{y}$) of spin-up and spin-down is shown in spin texture plot and the pitch of the PSH ($l_{PSH} = \frac{2\pi}{|\vec{Q}|} = \frac{\pi\hbar^2}{m_y^* \alpha}$) is calculated to be 11 nm which is approximately three times larger than that in CdTe (110) and ZnTe (110) structures²¹ and comparable to that in SnTe (001) thin films¹⁶. The factor of three comes from the comparative Rashba constant value as mentioned earlier. The spin projected band structure of MgTe ($+P_y$) is plotted in Figure 2(e) which shows energy bands along $\Gamma \rightarrow Y$ direction are degenerate. In this case, the SDLN is along the line $k_y = 0$ and can be seen from constant energy fermi surface plot in Figure 2(f).

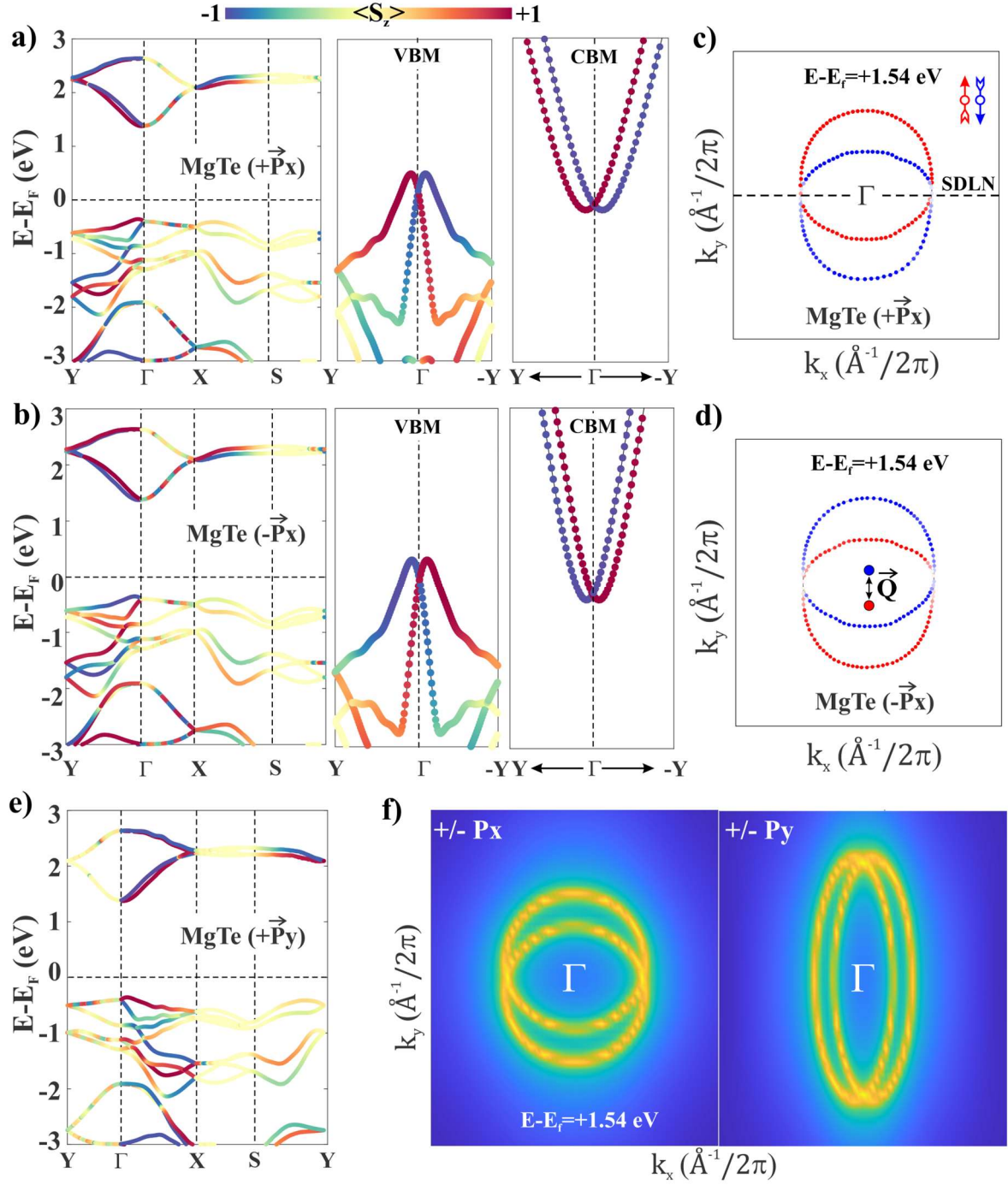


Figure 2 (a-b) spin-projected electronic band structure; the colour represents the projection of $\langle S_z \rangle$ on each band, (c-d) spin projected constant energy 2D contour plots calculated in the $k_x - k_y$ plane centred at the Γ -point; red/blue circles describe the orientation of spin along $\pm z$ direction; spin degenerate line node (SDLN) is indicated by a dashed line and the shifting wave vector between spin-up and the spin-down parabolic band is indicated by \vec{Q} , (e) spin projected band structure of MgTe having ferroelectric polarization along $+y$ -direction, (f) constant energy Fermi surface of MgTe system having ferroelectric polarization along $\pm x$ and $\pm y$ direction.

2.3 Origin of PST and Quantum Mechanical Phenomenon

To shed light on the origin of PST observed in this work, we need to revisit some of the proposed models. The PST is theoretically predicted in a 2D electron gas system with equal Rashba and Dresselhaus spin-orbit coupling parameters and was sought after in real materials. The concept of PST for application in non-ballistic spintronic devices is proposed by Schliemann et al.⁴ where the electrons are subjected to spin-orbit interaction of both Rashba and Dresselhaus type.²⁹ Including the linear terms of both Rashba and Dresselhaus contribution to the Hamiltonian for a 2D system is given by,^{5,29-31}

$$\mathcal{H} = \frac{p^2}{2m} + \mathcal{H}_R + \mathcal{H}_D \dots \dots \dots (3)$$

$$\mathcal{H} = \frac{\hbar^2 k^2}{2m} + \alpha(\sigma_x k_y - \sigma_y k_x) + \beta(\sigma_x k_x - \sigma_y k_y) \dots \dots \dots (4)$$

where \vec{k} is the momentum of the electron, α , and β correspond to the strengths of Rashba and Dresselhaus spin-orbit coupling respectively, m is the effective electron mass and σ_i is Pauli spin matrices. In the experiment, α and β can be tuned with an external electric field and sample geometry.⁴

The Hamiltonian in equation (4) takes the form;

$$\mathcal{H} = \begin{bmatrix} \frac{(k_x^2 + k_y^2)\hbar^2}{2m} & (ik_x + k_y)\alpha + (k_x + ik_y)\beta \\ (-ik_x + k_y)\alpha + (k_x - ik_y)\beta & \frac{(k_x^2 + k_y^2)\hbar^2}{2m} \end{bmatrix} \dots \dots \dots (5)$$

And diagonalizing the Hamiltonian gives the energy eigenvalues as;

$$E_{\pm} = \frac{\hbar^2(k_x^2 + k_y^2)}{2m} \pm \sqrt{k_x^2 \alpha^2 + k_y^2 \alpha^2 + 4k_x k_y \alpha \beta + k_x^2 \beta^2 + k_y^2 \beta^2} \dots \dots \dots (6)$$

For equal Rashba and Dresselhaus strength ($\alpha = \pm\beta$), a new type of SU(2) spin rotation symmetry is discovered⁶ that stabilizes the periodic precession of spin.^{4,6} In this condition, the spin state of the electrons becomes independent of the wave vector (k). Now simplifying the Hamiltonian with equal Rashba and Dresselhaus strength, the energy eigenvalues and corresponding energy states have been calculated and provided in Table 2.

Table 2 The energy eigenvalues and corresponding eigenstates of Hamiltonian having equal Rashba and Dresselhaus strength		
Cases	Eigen energy values	Eigen states
$\alpha = +\beta$	$E_1 = \frac{\hbar^2(k_x^2 + k_y^2)}{2m} - \sqrt{2}\alpha(k_x + k_y)$	$\begin{pmatrix} -\frac{(1+i)(k_x + k_y)}{\sqrt{2}} \\ 1 \end{pmatrix}$
	$E_2 = \frac{\hbar^2(k_x^2 + k_y^2)}{2m} + \sqrt{2}\alpha(k_x + k_y)$	$\begin{pmatrix} \frac{(1+i)(k_x + k_y)}{\sqrt{2}} \\ 1 \end{pmatrix}$

$\alpha = -\beta$	$E_3 = \frac{\hbar^2(k_x^2 + k_y^2)}{2m} - \sqrt{2}\alpha(k_x - k_y)$	$\left(\frac{(1-i)(k_x - k_y)}{\sqrt{2}} \right)$
	$E_4 = \frac{\hbar^2(k_x^2 + k_y^2)}{2m} + \sqrt{2}\alpha(k_x - k_y)$	$\left(-\frac{(1-i)(k_x - k_y)}{\sqrt{2}} \right)$

The energy dispersion relations listed in Table 2 for both cases $\alpha = \pm\beta$ are plotted in Figure 3(a) which provides a qualitative understanding of the quantum mechanical phenomenon as follows. The energy dispersion of E_{\pm} as in eq. (6) takes the complex form whereas for $\alpha = \pm\beta$; $E_{1/2}$ and $E_{3/4}$ are perfect parabolas. A spin degenerate line node and the shifting wave vector $\vec{Q} = \frac{\sqrt{2}m\alpha}{\hbar^2}(1, \pm 1)$ between spin-up and spin-down parabolic bands can be observed which is consistent with the literature.⁵

For $\alpha = \pm\beta$, the diagonalized Hamiltonian as presented in equation (5) is mathematically equivalent to the Hamiltonian of [110] Dresselhaus model⁶ and is given by;

$$\mathcal{H}_{[110]} = \frac{k_x^2 + k_y^2}{2m} - 2\alpha k_x \sigma_z \dots\dots\dots (7)$$

The energy eigenvalues and corresponding eigenstates ($\psi_{\vec{k}}$) of eq. (7) are given by $\left\{ \left\{ E_5 = \frac{\hbar^2(k_x^2 + k_y^2)}{2m} - 2\alpha k_x \right\}, \left\{ E_6 = \frac{\hbar^2(k_x^2 + k_y^2)}{2m} + 2\alpha k_x \right\} \right\}$ and $\left\{ \begin{pmatrix} 1 \\ 0 \end{pmatrix}, \begin{pmatrix} 0 \\ 1 \end{pmatrix} \right\}$, respectively. The spin polarization of each eigenstate can be obtained by $\vec{S} = \langle \psi_{\vec{k}} | \vec{\sigma} | \psi_{\vec{k}} \rangle$ and is given by $\left\{ \begin{pmatrix} 0 \\ 0 \\ 1 \end{pmatrix}, \begin{pmatrix} 0 \\ 0 \\ -1 \end{pmatrix} \right\}$. This model is relatively simple compared to the former model.

Is it a coincidence that (110) facets of MgTe exhibit PST and how is the Hamiltonian in equation (7) related to these 2D structures? To get an answer, we note that these 2D Rashba semiconductors are ferroelectric and are confined along the (110) plane. The in-plane electric field (E_x) can generate a unidirectional spin-orbit-field (SOF) in a 2D material expressed by;^{15,16}

$$\vec{\Omega}_{SOF}(\vec{k}) = \alpha(\hat{E}_x \times \vec{k}) = \alpha k_y \hat{z} \dots\dots\dots (8)$$

Eq. (8) indicates that the spin polarization direction is along the +z axis whereas the magnitude of spin splitting depends on the Rashba constant (α).

Now we need to analyze the dependence of observable spin states with respect to ferroelectric polarization direction (\hat{P}). For a ferroelectric material, an electric field (\hat{E}) in eq. (8) can be replaced with \hat{P} and for ferroelectric polarization along +x axis i.e., $+\hat{P}_x$, the effective Hamiltonian including the SOC term can be written as eq. (9) which takes the identical form to that of [110] Dresselhaus model as in equation (7);

$$\mathcal{H} = \mathcal{H}_{kin} + \vec{\Omega}_{SOF} \cdot \vec{\sigma} = \frac{\hbar^2}{2m}(k_x^2 + k_y^2) + \alpha k_y \sigma_z \dots\dots\dots (9)$$

The energy eigenvalues and eigenvectors/states ($\psi_{\vec{k}}$) can be obtained by diagonalizing the Hamiltonian in eq. (9) and are listed in Table 3.

Table 3 The energy eigen values, eigenstates and corresponding spin polarization for 2D system having ferroelectric polarization direction along $+\hat{P}_x$		
Eigen energy values	Eigenvectors	Spin polarization in the form of $\begin{pmatrix} S_x \\ S_y \\ S_z \end{pmatrix}$
$E_7 = \frac{\hbar^2(k_x^2 + k_y^2)}{2m} + \alpha k_y$	$\begin{pmatrix} 1 \\ 0 \end{pmatrix}$	$\begin{pmatrix} 0 \\ 0 \\ 1 \end{pmatrix}$
$E_8 = \frac{\hbar^2(k_x^2 + k_y^2)}{2m} - \alpha k_y$	$\begin{pmatrix} 0 \\ 1 \end{pmatrix}$	$\begin{pmatrix} 0 \\ 0 \\ -1 \end{pmatrix}$

Similarly for ferroelectric polarization along the -x axis i.e., $-\hat{P}_x$, the effective Hamiltonian including the SOC term can be written as eq. (10) and its eigenvalues, eigenstates, and spin polarization are listed in Table 4.

$$\mathcal{H} = \frac{\hbar^2}{2m}(k_x^2 + k_y^2) - \alpha k_y \sigma_z \dots\dots\dots (10)$$

Table-4 The energy eigenvalues, eigenstates, and corresponding spin polarization for 2D system having ferroelectric polarization direction along $-\hat{P}_x$		
Eigen energy values	Eigen states	Spin polarization in the form of $\begin{pmatrix} S_x \\ S_y \\ S_z \end{pmatrix}$
$E_9 = \frac{\hbar^2(k_x^2 + k_y^2)}{2m} - \alpha k_y$	$\begin{pmatrix} 1 \\ 0 \end{pmatrix}$	$\begin{pmatrix} 0 \\ 0 \\ 1 \end{pmatrix}$
$E_{10} = \frac{\hbar^2(k_x^2 + k_y^2)}{2m} + \alpha k_y$	$\begin{pmatrix} 0 \\ 1 \end{pmatrix}$	$\begin{pmatrix} 0 \\ 0 \\ -1 \end{pmatrix}$

A comparative analysis between energy expressions listed in Table 3 and Table 4 indicates that for a given energy dispersion, the eigenstate and the spin polarization of the eigenstate are completely reversed. Now, the energy equations listed in Table 3 and Table 4 are plotted in Figure 3(b), which provides the essential information about the quantum mechanical system studied in this work. The SDLN is along the line $k_x = 0$ i.e., in the direction of ferroelectric polarization ($\pm\hat{P}_x$) whereas the shift vector \vec{Q} is along [010]. The reversible nature of spin-polarization of energy states with ferroelectric polarization can also be depicted in Figure 3(b) and the same can be compared from Table 3 and Table 4. These analytical results match exactly with the DFT results obtained in the above section.

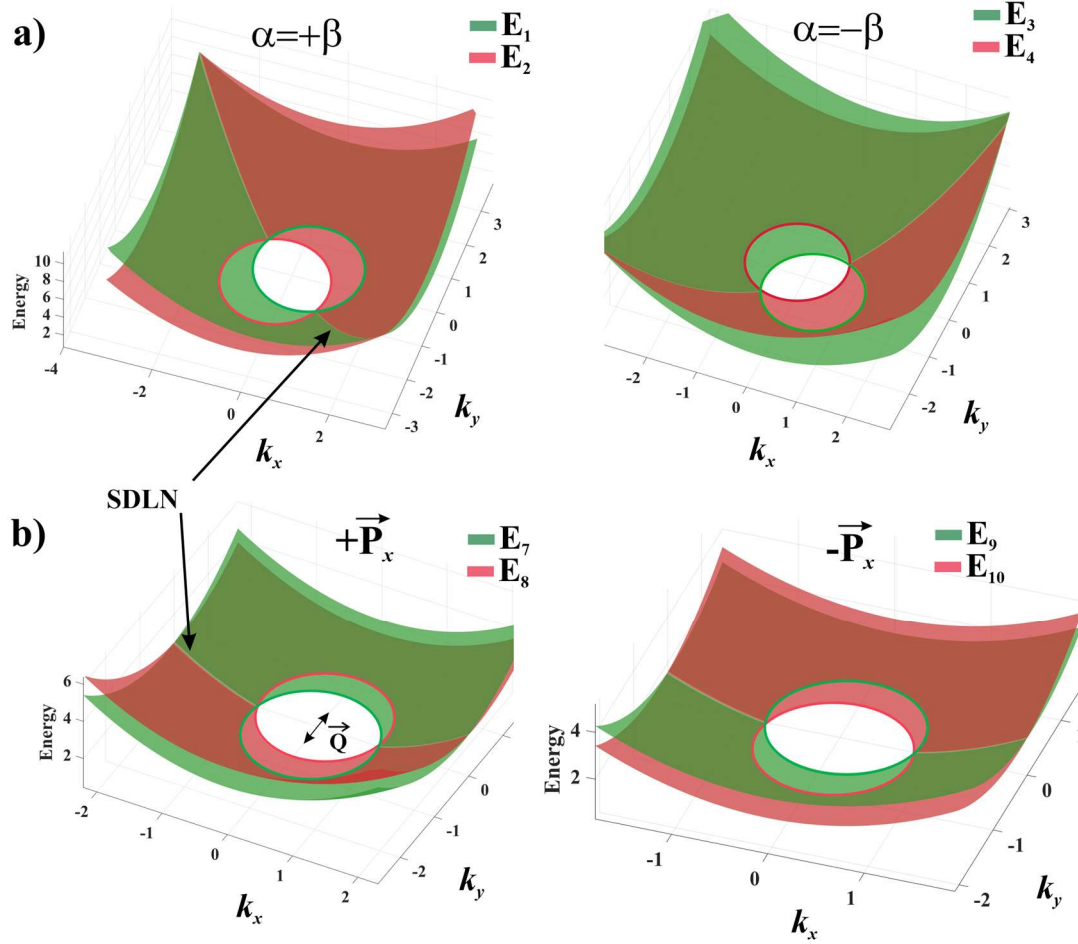


Figure 3. 3D view of energy dispersions obtained from different Hamiltonian; spin degenerate line nodes (SDLN) and shift vector (\vec{Q}) are indicated. Here $\hbar = m = 1, \alpha = 0.2, k_x = k_y = [-\pi, +\pi]$ are used for plotting.

Now from the symmetry point of view, a $k.p$ Hamiltonian³² is constructed for a symmorphic 2D crystal structure with the following symmetry operations; one two-fold rotational symmetry C_{2x} around x -axis, time reversal symmetry and mirror symmetry in y . The Hamiltonian in eq. (11) takes a similar form to that of Rashba Hamiltonian which indicates a symmorphic crystal structure exhibiting the Rashba effect. The Hamiltonian and energy dispersion relations for the 2D Rashba model are provided in SI.

$$\mathcal{H} = \varphi(k_x^2 + k_y^2) + \delta(\sigma_x k_y + \sigma_y k_x) \dots\dots\dots (11)$$

Here φ and δ are arbitrary constants.

2.4 Magnetic element-free nonballistic spin-field effect transistor

In the previous section, we have shown that these structures exhibit PST and hence can be an ideal material for nonballistic s-FET. In this section, we have discussed the application of MgTe (110) structures in a spin-Hall transistor. To circumvent the limitations that exist in

conventional s-FET such as pure spin current generation, spin injection, and detection efficiencies at the interfaces between ferromagnet and channel semiconductor, a schematic of an all-electric spin-Hall transistor (SHT)³³ is presented in Figure 4. The operation of such devices relies on different mechanisms such as the spin-Hall effect (SHE) and inverse spin-Hall effect (ISHE). The SHT consists of only one material with three regions. The direct SHE converts the charge current flowing along the y -direction to a transverse spin-current along the x -direction where the spin polarization is along the z -axis given by;

$$I_s \propto \vartheta \times I_c \dots\dots (12)$$

where ϑ is the spin polarization direction and I_s/I_c is the flow of spin/charge current. Thus, the pure spin current moving along the x -axis is injected into region M-II. The spins polarized along the z -axis are efficiently injected from M-I to M-II without loss owing to no interface in between. The spin does not lose any information for $E_z = 0$. However, previous reports indicate the breaking of PSH mode under finite vertical electric field $E_z \neq 0$,^{18,21} hence region M-II controls the injected spin current. The gate-modulated spins in M-II are now injected into the region M-III where the ISHE converts the spin-current ($+x$) into a transverse charge current ($-y$) given by equation (13) which generates a Hall voltage (V_H) along the y -direction.³⁴

$$I_c \propto \vartheta \times I_s \dots\dots\dots (13)$$

Equations (12-13) are reminiscent of the Lorentz force in electromagnetics. Unlike conventional s-FET, no interface between regions M-II and M-III guarantees an efficient detection of spin information. These three processes provide an essential platform to generate, manipulate, and detect the spins without involving ferromagnets or external magnetic fields. Thus, the Hall voltage in M-III can be controlled in region M-II with an out-of-plane electric field.^{35,36} To show the independence of PST with layer thickness, a 3L-MgTe structure is designed, and a spin-projected band structure is plotted in Figure S3 which depicts the symmetry-protected properties are very robust. The spin-Hall conductivity of multilayer structures 2L and 3L MgTe systems are calculated and plotted in Figure 4. The spin Hall conductivity (SHC) is a measure of the spin Hall effect (SHE) which originates from the coupling between charge and spin degrees of freedom due to spin-orbit interaction.^{37,38} The SOC transforms longitudinal charge flow into transverse spin current without any external magnetic field. The SHC projected band structure and k -point resolved SHC are plotted in Figure 4(b) which depicts a finite SHC observed at both CBM and VBM. The SHC is found to be concentrated around the Γ -point of the rectangular Brillouin zone.³⁹

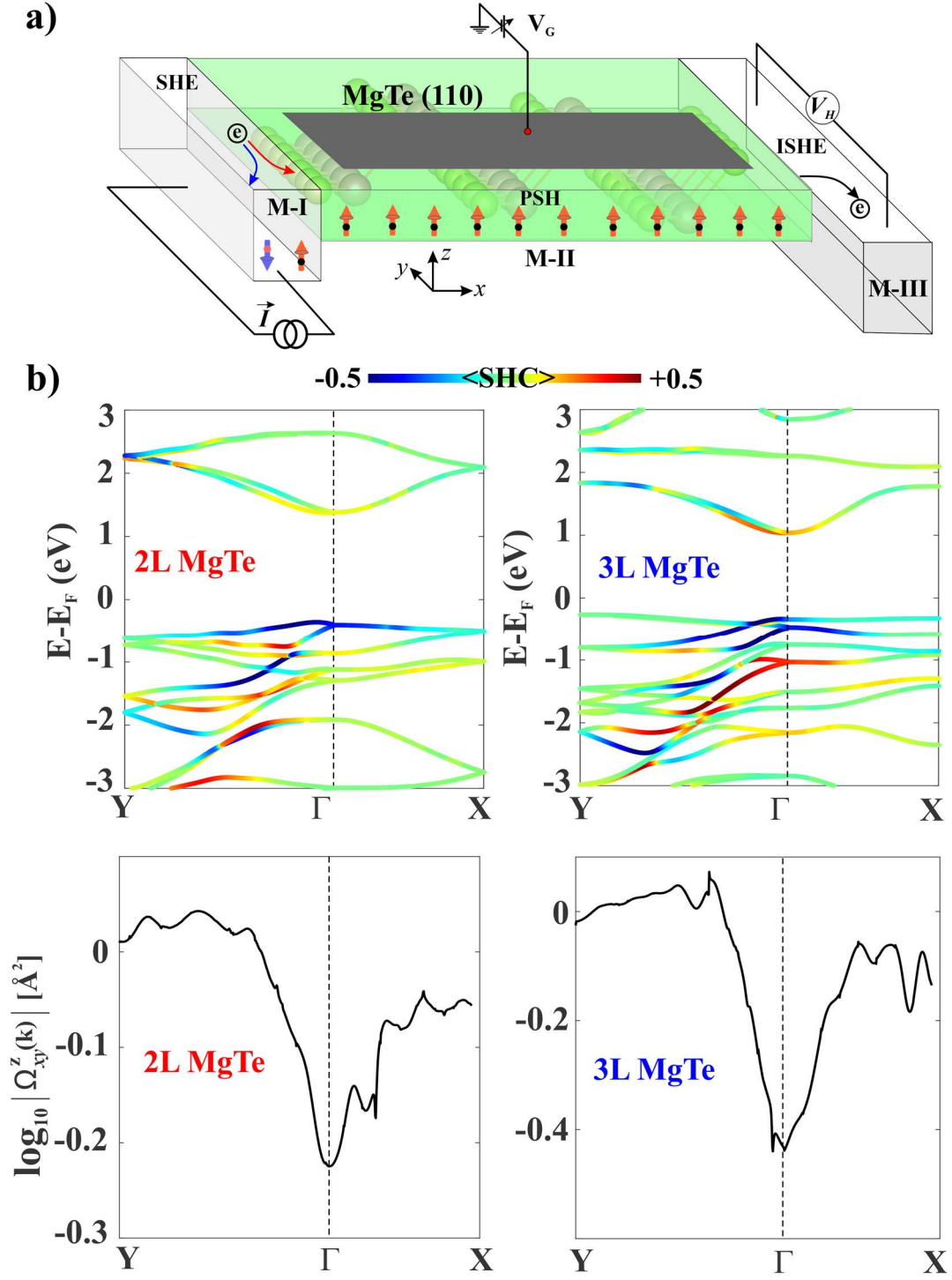


Figure 4 (a) Schematic of spin-Hall effect transistor based on (110) facets of MgTe, (b) SHC projected band structure and k -point resolved SHC for 2L and 3L MgTe.

3. Conclusion

In conclusion, we have demonstrated that (110) facets of zinc-blende MgTe 2D structures possess a unique combination of the three basic transformations found in nature; rotation, mirror reflection, and translation and thus exhibit uncommon properties with respect to its parent bulk structure or other facets. The in-plane ferroelectric polarization with SOC brings unconventional momentum-independent unidirectional spin polarization. To understand the origin of such exquisite properties in this particular facet, a simple quantum mechanical model is presented and solved using an analytical method. The results obtained from the analytical method match exactly with that obtained from DFT. Further, the PST is found to be independent of layer thickness. Both monolayer and multilayer structures exhibit a finite spin-Hall-conductivity at the band edges and are mostly localized at the Γ -point. Although the MgTe (110) has been studied for many years in optoelectronic devices, this work provides an in-depth analysis and sheds light on its practical application in nonballistic spin-field effect transistors which has not yet been explored but has utmost scientific and technological importance. The future of spintronics lies in the realization of ferromagnet-free nonballistic s-FET using 2D semiconductors that exhibit symmetry-protected PST intrinsically such as MgTe (110) proposed in this work. Moreover, the application of MgTe (110) structures in a ferromagnet-free non-ballistic spin field effect transistor is the central proposal of this work.

4. Computational details:

All the theoretical calculations are performed within the framework of density functional theory (DFT) embedded in the VASP code^{40,41} with the Perdew-Burke-Ernzerhof generalized gradient approximation (GGA-PBE).⁴² The projector-augmented plane waves (PAW) have been adopted to describe the ion-electron interaction.⁴³ The plane wave cut-off of 520 eV is used with the energy convergence criteria of 10^{-8} eV for self-consistent calculations. A Γ -centered k -point mesh of $15 \times 15 \times 1$ is used to sample the Brillouin zone (BZ). A vacuum space of more than 20 \AA is added to avoid periodic interaction along the z -direction. PYPROCAR is used to plot spin texture.⁴⁴ The ferroelectric properties are calculated using the Berry phase method.⁴⁵⁻⁴⁷ The spin Hall conductivity (SHC) is calculated from Berry curvature using a dense $150 \times 150 \times 1$ k -mesh based on maximally localized Wannier function^{39,48} using Quantum Espresso⁴⁹ and Wannier90^{50,51} code by the formula^{52,53};

$$\sigma_{xy}^z = \frac{e}{\hbar} \int_{BZ} \frac{dk}{(2\pi)^2} \Omega^z(k)$$

$\Omega^z(k)$ is the k -resolved term which is given by $\Omega^z(k) = \sum_n f_{kn} \Omega_n^z(k)$. Here, f_{kn} is the Fermi-Dirac distribution function for the n th band at k and $\Omega_n^z(k)$ is an analogue of the Berry curvature for the n th band given as;

$$\Omega_n^z(k) = \sum_{n' \neq n} \frac{2 \text{Im}[\langle kn | j_x^z | kn' \rangle \langle kn' | v_y | kn \rangle]}{(\epsilon_{kn} - \epsilon_{kn'})^2}$$

Here, $j_x^z = \frac{1}{2} \{s_z, v\}$ is the spin current operator, $s_z = \frac{\hbar}{2} \sigma^z$ is the spin operator, v is the velocity operator and $|kn\rangle$ is the wave function of energy ϵ_{kn} .

Acknowledgment

MKM and PJ acknowledge financial support from the U.S. Department of Energy, Office of Basic Energy Sciences, Division of Materials Sciences and Engineering under Award No. DE-FG02-96ER45579. Resources of the National Energy Research Scientific Computing (NERSC) Center supported by the Office of Science of the U.S. Department of Energy under Contract No. DE-AC02-05CH11231 is also acknowledged. The authors extend their acknowledgment to the High-Performance Research Computing (HPRC) core facility at Virginia Commonwealth University for providing supercomputing resources.

References:

1. Datta, S. & Das, B. Electronic analog of the electro-optic modulator. *Appl. Phys. Lett.* **56**, 665–667 (1990).
2. Datta, S. How we proposed the spin transistor. *Nat. Electron.* **1**, 604–604 (2018).
3. Chen, J., Wu, K., Hu, W. & Yang, J. Spin–Orbit Coupling in 2D Semiconductors: A Theoretical Perspective. *J. Phys. Chem. Lett.* **12**, 12256–12268 (2021).
4. Schliemann, J., Egues, J. C. & Loss, D. Nonballistic Spin-Field-Effect Transistor. *Phys Rev Lett* **90**, 146801 (2003).
5. Schliemann, J. Colloquium: Persistent spin textures in semiconductor nanostructures. *Rev Mod Phys* **89**, 011001 (2017).
6. Bernevig, B. A., Orenstein, J. & Zhang, S.-C. Exact SU(2) Symmetry and Persistent Spin Helix in a Spin-Orbit Coupled System. *Phys Rev Lett* **97**, 236601 (2006).
7. Koralek, J. D. *et al.* Emergence of the persistent spin helix in semiconductor quantum wells. *Nature* **458**, 610–613 (2009).
8. Walser, M. P., Reichl, C., Wegscheider, W. & Salis, G. Direct mapping of the formation of a persistent spin helix. *Nat. Phys.* **8**, 757–762 (2012).
9. Kohda, M. *et al.* Gate-controlled persistent spin helix state in (In,Ga)As quantum wells. *Phys Rev B* **86**, 081306 (2012).
10. Sasaki, A. *et al.* Direct determination of spin–orbit interaction coefficients and realization of the persistent spin helix symmetry. *Nat. Nanotechnol.* **9**, 703–709 (2014).

11. Ohno, M. & Yoh, K. Datta-Das-type spin-field-effect transistor in the nonballistic regime. *Phys Rev B* **77**, 045323 (2008).
12. Choudhuri, I., Bhauriyal, P. & Pathak, B. Recent Advances in Graphene-like 2D Materials for Spintronics Applications. *Chem. Mater.* **31**, 8260–8285 (2019).
13. Eberle, F. *et al.* Controlled Rotation of Electrically Injected Spins in a Nonballistic Spin-Field-Effect Transistor. *Nano Lett.* **23**, 4815–4821 (2023).
14. Tao, L. L. & Tsymbal, E. Y. Persistent spin texture enforced by symmetry. *Nat. Commun.* **9**, 2763 (2018).
15. Absor, Moh. A. U. & Ishii, F. Intrinsic persistent spin helix state in two-dimensional group-IV monochalcogenide MX monolayers (M=Sn or Ge and X=S, Se, or Te). *Phys Rev B* **100**, 115104 (2019).
16. Lee, H., Im, J. & Jin, H. Emergence of the giant out-of-plane Rashba effect and tunable nanoscale persistent spin helix in ferroelectric SnTe thin films. *Appl. Phys. Lett.* **116**, 022411 (2020).
17. Absor, M. A. U. *et al.* Highly persistent spin textures with giant tunable spin splitting in the two-dimensional germanium monochalcogenides. *J. Phys. Condens. Matter* **33**, 305501 (2021).
18. Jin, K.-H., Oh, E., Stania, R., Liu, F. & Yeom, H. W. Enhanced Berry Curvature Dipole and Persistent Spin Texture in the Bi(110) Monolayer. *Nano Lett.* **21**, 9468–9475 (2021).
19. Sun, Y. *et al.* Fabrication of flexible and freestanding zinc chalcogenide single layers. *Nat. Commun.* **3**, 1057 (2012).
20. Soares, E. A., Carvalho, V. E. de & Nascimento, V. B. A layer-by-layer study of CdTe(110) surface Debye temperature and thermal vibrations by low energy electron diffraction. *Surf. Sci.* **431**, 74–83 (1999).
21. Mohanta, M. K. & Jena, P. Symmetry-driven persistent spin texture for the two-dimensional nonsymmorphic CdTe and ZnTe crystal structures. *Phys Rev B* **108**, 085432 (2023).

22. Kepenekian, M. *et al.* Rashba and Dresselhaus Effects in Hybrid Organic–Inorganic Perovskites: From Basics to Devices. *ACS Nano* **9**, 11557–11567 (2015).
23. Mohanta, M. K., Arora, A. & De Sarkar, A. Conflux of tunable Rashba effect and piezoelectricity in flexible magnesium monochalcogenide monolayers for next-generation spintronic devices. *Nanoscale* **13**, 8210–8223 (2021).
24. Mohanta, M. K., IS, F., Kishore, A. & De Sarkar, A. Spin-Current Modulation in Hexagonal Buckled ZnTe and CdTe Monolayers for Self-Powered Flexible-Piezo-Spintronic Devices. *ACS Appl. Mater. Interfaces* **13**, 40872–40879 (2021).
25. Singh, S. & Romero, A. H. Giant tunable Rashba spin splitting in a two-dimensional BiSb monolayer and in BiSb/AlN heterostructures. *Phys Rev B* **95**, 165444 (2017).
26. Sheoran, S., Monga, S., Phutela, A. & Bhattacharya, S. Coupled Spin-Valley, Rashba Effect, and Hidden Spin Polarization in WSi₂N₄ Family. *J. Phys. Chem. Lett.* **14**, 1494–1503 (2023).
27. Ahammed, R. *et al.* Ultrahigh Out-of-Plane Piezoelectricity Meets Giant Rashba Effect in 2D Janus Monolayers and Bilayers of Group IV Transition-Metal Trichalcogenides. *J. Phys. Chem. C* **124**, 21250–21260 (2020).
28. Autieri, C., Barone, P., Slawińska, J. & Picozzi, S. Persistent spin helix in Rashba-Dresselhaus ferroelectric CsBiNb₂O₇. *Phys Rev Mater* **3**, 084416 (2019).
29. Dresselhaus, G. Spin-Orbit Coupling Effects in Zinc Blende Structures. *Phys Rev* **100**, 580–586 (1955).
30. Bychkov, Y. A. & Rashba, É. I. Properties of a 2D electron gas with lifted spectral degeneracy. *JETP Lett* **39**, 78 (1984).
31. Maurer, B., Vorwerk, C. & Draxl, C. Rashba and Dresselhaus effects in two-dimensional Pb-I-based perovskites. *Phys Rev B* **105**, 155149 (2022).
32. Varjas, D., Rosdahl, T. Ö. & Akhmerov, A. R. Qsymm: algorithmic symmetry finding and symmetric Hamiltonian generation. *New J. Phys.* **20**, 093026 (2018).

33. Choi, W. Y. *et al.* Ferromagnet-Free All-Electric Spin Hall Transistors. *Nano Lett.* **18**, 7998–8002 (2018).
34. Miao, B. F., Huang, S. Y., Qu, D. & Chien, C. L. Inverse Spin Hall Effect in a Ferromagnetic Metal. *Phys Rev Lett* **111**, 066602 (2013).
35. Wunderlich, J. *et al.* Spin Hall Effect Transistor. *Science* **330**, 1801–1804 (2010).
36. Wunderlich, J. *et al.* Spin-injection Hall effect in a planar photovoltaic cell. *Nat. Phys.* **5**, 675–681 (2009).
37. Dyakonov, M. I. Possibility of orienting electron spins with current. *JETP Lett USSR* **13**, 467 (1971).
38. Dyakonov, M. I. & Perel, V. I. Current-induced spin orientation of electrons in semiconductors. *Phys. Lett. A* **35**, 459–460 (1971).
39. Qiao, J., Zhou, J., Yuan, Z. & Zhao, W. Calculation of intrinsic spin Hall conductivity by Wannier interpolation. *Phys Rev B* **98**, 214402 (2018).
40. Kresse, G. & Furthmüller, J. Efficient iterative schemes for ab initio total-energy calculations using a plane-wave basis set. *Phys. Rev. B* **54**, 11169–11186 (1996).
41. Kresse, G. & Furthmüller, J. Efficiency of ab-initio total energy calculations for metals and semiconductors using a plane-wave basis set. *Comput. Mater. Sci.* **6**, 15–50 (1996).
42. Perdew, J. P., Burke, K. & Ernzerhof, M. Generalized Gradient Approximation Made Simple. *Phys. Rev. Lett.* **77**, 3865–3868 (1996).
43. Blöchl, P. E. Projector augmented-wave method. *Phys. Rev. B* **50**, 17953–17979 (1994).
44. Herath, U. *et al.* PyProcar: A Python library for electronic structure pre/post-processing. *Comput. Phys. Commun.* **251**, 107080 (2020).
45. Resta, R. Theory of the electric polarization in crystals. *Ferroelectrics* **136**, 51–55 (1992).
46. Resta, R. Macroscopic polarization in crystalline dielectrics: the geometric phase approach. *Rev Mod Phys* **66**, 899–915 (1994).

47. King-Smith, R. D. & Vanderbilt, D. Theory of polarization of crystalline solids. *Phys Rev B* **47**, 1651–1654 (1993).
48. Damle, A., Lin, L. & Ying, L. SCDM-k: Localized orbitals for solids via selected columns of the density matrix. *J. Comput. Phys.* **334**, 1–15 (2017).
49. Giannozzi, P. *et al.* QUANTUM ESPRESSO: a modular and open-source software project for quantum simulations of materials. *J. Phys. Condens. Matter* **21**, 395502 (2009).
50. Mostofi, A. A. *et al.* wannier90: A tool for obtaining maximally-localised Wannier functions. *Comput. Phys. Commun.* **178**, 685–699 (2008).
51. Pizzi, G. *et al.* Wannier90 as a community code: new features and applications. *J. Phys. Condens. Matter* **32**, 165902 (2020).
52. Guo, G. Y., Murakami, S., Chen, T.-W. & Nagaosa, N. Intrinsic Spin Hall Effect in Platinum: First-Principles Calculations. *Phys Rev Lett* **100**, 096401 (2008).
53. Xu, X., Zhang, L., Zou, L., Li, M. & Wang, H. Regulating Interfacial Spin Hall Conductivity with Ferroelectricity. *J. Phys. Chem. Lett.* **13**, 3310–3316 (2022).